


Two-dimensional Janus IT - $CrXY$ ($X = S, Se, Te, Y = F, Cl, Br, I$): Multifunctional ferromagnetic semiconductor with large valley and piezoelectric polarizations

Jianke Tian,¹ Jia Li^{1,*}, Hengbo Liu¹, Yan Li,¹ and Junjie Shi²

¹*School of Science, Hebei University of Technology, Tianjin 300401, People's Republic of China*

²*State Key Laboratory for Artificial Microstructures and Mesoscopic Physics, School of Physics, Peking University Yangtze Delta Institute of Optoelectronics, Peking University, 5 Yiheyuan Street, Beijing 100871, People's Republic of China*

 (Received 23 November 2023; revised 14 January 2024; accepted 26 February 2024; published 12 March 2024)

Ferrovalley, spin, and piezoelectric polarizations are novel characteristics for electronic materials, and so far, there are few reports that these properties coexist in a single system. By first-principles calculations, we predict a series of highly stable intrinsic ferrovalley materials, i.e., single layer $CrXY$ ($X = S, Se, Te, Y = F, Cl, Br, I$) with large valley polarization up 76.1 meV and appropriate Curie temperature higher than room temperature. For $CrSF$, the large bandgap of spin-up (spin-down) is as high as 1.96 eV (3.11 eV), which is beneficial for generating 100% spin polarized carriers by optical excitation or electrical gating. The quasianomalous valley Hall effect with valley contrast properties can be induced by compressive strain in $CrSI$ and $CrTeX$ ($X = Cl, Br, I$). Meanwhile, the large in-plane ($-5.78 - 3.54$ pm/V) and outside plane piezoelectric polarization ($-5.03 - 2.53$ pm/V) of $CrXY$ are higher than most reported two-dimensional materials. Our work provides a pathway for a wide variety of applications in nanoelectronics, spintronics, valleytronics, piezoelectrics, and other demanding areas.

DOI: [10.1103/PhysRevB.109.125413](https://doi.org/10.1103/PhysRevB.109.125413)

I. INTRODUCTION

Since graphene was successfully stripped, two-dimensional (2D) materials have been widely concerned because of their unique physical properties [1–3]. It has been proved by the Mermin-Wagner theorem that 2D long-range magnetic ordering can be suppressed due to the thermal fluctuations, which limits the development of 2D magnetic materials [4]. However, it has been found that 2D CrI_3 [5] and VI_3 [6] show an intrinsic ferromagnetic (FM) ordering at the Curie temperature (T_c) 45 and 49 K, respectively. This discovery has aroused widespread concern about the 2D magnetic materials [7]. The valleytronics, related to energy valley of band structure, is truly flourishing with the advent of 2D magnetic materials [8–10]. The valley is referred to two or more energy extremes located in the valence or conduction bands. Similar to the charge and spin of electrons, valley degrees of freedom can be also used to encode, store, and manipulate information [11]. The current studies about valley mainly focus on 2D hexagonal materials, such as 2H-phase transition metal dichalcogenides (TMDs) MX_2 ($M = Mo, W, X = S, Se, Te$) due to their valley-contrasting physics [12]. The unique structure and strong spin orbital coupling (SOC) effect of TMDs leads to the spatial inversion-symmetry-broken and degenerate but not equivalent valleys at K and K' in momentum space. Especially, the large distance between two unequal valleys will inhibit the intervalley scattering from smooth deformations and low-energy phonons [13–16]. Therefore,

valley as a new degree of freedom, is expected to be applied to the next generation of electronic devices.

However, to realize the application of valleytronics, it is necessary to break the energy degeneracy between the valleys. Due to the absence of magnetism in single layer (SL) TMDs, the valley in momentum space remains degenerate in energy due to the protection of time-reversal symmetry, which greatly limits the application of TMDs [13–15]. In view of this situation, many strategies to break valley degeneracy and realize valley polarization have been proposed. Optical pumping [17,18] is a dynamic process of exciting carriers, which is widely used to achieve valley polarization. However, due to the short lifetime of the induced carriers, it is unsuitable for valleytronic applications. Although the valley polarization can be induced by the external magnetic field [19–21], its induction efficiency is very low (0.1 – 0.2 meV/T), and the valley polarization will disappear with the removal of the external magnetic field. The method of magnetic doping [22] will increase scattering during carrier transmission. The substrate introduced in the magnetic proximity effect [23,24] will enlarge the size of the device and increase the energy consumption. Thus, it is important to find intrinsic valley polarization. Recently, the 2D ferrovalley materials with spontaneous valley polarization were proposed, which provides a new scheme for the fabrication of electronic devices [25]. Although some ferrovalley materials have been reported, such as VSe_2 [25,26], $LaBr_2$ [27], GdX_2 ($X = Cl, Br$) [28], MBr_2 ($M = Ru, Os$) [29], VSi_2N_4 [30], $FeClBr$ [31], and MA_2Z_4 ($M =$ transition metal, $A = Si, Ge, Z = N, P, As$) [32,33], the promising candidates with high valley polarization are still very rare. Moreover, most candidate materials face issues such as smaller valley polarization and lower magnetic transition temperature. Compared with the H-phase materials, the study

*Corresponding author: jiali@hebut.edu.cn

about T-phase materials is rare because the degeneracy of the valley is protected by the spatial inversion symmetry of the T-phase system. Therefore, it is crucial to expand valleytronic materials and search for 2D ferrovalley materials with significant valley splitting and high T_c for the integration of various electronic functions. Similar to valley polarization for valleytronics, piezoelectric polarization reflecting the electronic output in response of the mechanical stimulation is crucial for the application of piezoelectric materials [34,35]. From the discovery of the piezoelectricity of 2D MoS₂ [36] to the confirmed enormous piezoelectricity of 2D SnSe [37,38] and CrXY ($X \neq Y = S, Se, Te$) [39], studies have been piled up to searching for large piezoelectric materials. Because of the unique photoresponse under polarized light in valleytronic materials [40], the ferrovalley materials may be also ideal for piezophotonics, where charges originating from piezoelectric effects can be coupled with polarized light to modulate the charge-carrier generation, separation and recombination in semiconducting nanostructures and solar cells [41]. The excellent piezoelectric properties can be obtained by breaking the mirror symmetry and space-inversion symmetry of materials [42]. In recent years, the Janus MoSSe structure was successfully manufactured by replacing the S (Se) layer in the MoS₂ (MoSe₂) structure with the Se (S) layer through chemical vapor deposition [43,44]. Inspired by this structure, we replace a layer of X atoms in T-phase CrX₂ ($X = S, Se, Te$) with Y ($Y = F, Cl, Br, I$) atoms to break the spatial inversion symmetry, which may lead to spontaneous valley polarization and excellent piezoelectric properties. We believe that Janus SL CrXY ($X = S, Se, Te, Y = F, Cl, Br, I$) can be realized in the future.

In this work, using first-principles calculations, we propose a series of stable 2D ferrovalley CrXY ($X = S, Se, Te, Y = F, Cl, Br, I$) materials. The results show that SL CrXY is a semiconductor with a band gap locating at the K/K' or high symmetric paths, forming two or multiple energy valleys. Due to the strong SOC of Cr, a maximum valley splitting of -76.1meV can be observed in SL CrTeCl. All the SL CrXY show FM semiconductor character and the T_c of most of SL CrXY is greater than 300 K. Biaxial strain can effectively regulate the magnetic anisotropy energy (MAE), enhance valley polarization, and induce quasianomalous valley Hall effect (AVHE). The piezoelectric properties d_{11} ($-5.78 - 3.54\text{pm/V}$) and d_{31} ($-5.03 - 2.53\text{pm/V}$) of SL CrXY are higher than most of reported 2D materials (less than 2pm/V). Our work suggests that SL CrXY are outstanding ferrovalley materials in integrated nanodevices of electronics, spintronics, valleytronics, and piezoelectrics.

The rest of this paper is organized as follows. In the next section, we give our computational details and methods. In the next few sections, we present atomic structures and stability, magnetic properties and T_c , electronic band structures, AVHE, quasi-AVHE and piezoelectric properties of SL CrXY. Finally, we give our conclusion.

II. COMPUTATIONAL DETAILS

All structural optimization and electronic structure calculations are performed using the projector augmented wave method [45,46] through the Vienna *ab initio* simulation

package (VASP) [47,48]. For exchange and correlation interactions, the generalized gradient approximation of Perdew-Burke-Ernzerhof functional (PBE) is treated [49]. The kinetic energy cutoff and total energy convergence criterion is set to 500 eV and 10^{-6} eV, respectively. Atomic positions are fully relaxed until the maximum force on each atom is less than 0.01eV/\AA . A 20\AA vacuum layer in the z direction is used to eliminate interactions between adjacent layers. The Monkhorst-Pack grid is chosen to be Γ centered $11 \times 11 \times 1$ for electronic structure and $8 \times 14 \times 1$ for piezoelectric stress tensors e_{ij} . To better describe the strong correlation effect for Cr atoms, a Hubbard correction $U_{\text{eff}} = 2.1\text{eV}$ is employed within the rotationally invariant approach [50,51]. The SOC effect [52] is included in the calculations. The VASP data are processed by VASPKIT code [53]. The phonon dispersion is based on a $4 \times 4 \times 1$ supercell by using the PHONOPY code [54]. *Ab initio* molecular dynamic (AIMD) simulations adopt the NVT ensemble based on the Nosé-Hoermostat [55] at 300 K with a total of 6.0 ps. The T_c of the SL CrXY are estimated by using the Monte Carlo (MC) simulation package MCSOLVER [56] based on the Metropolis algorithm. The elastic stiffness and piezoelectric stress tensors (C_{ij} and e_{ij}) are calculated by using strain-stress relationship (SSR) and density-functional perturbation theory (DFPT) method. The Berry curvatures of SL CrXY is calculated using maximally localized Wannier functions implemented in WANNIER90 [57].

III. RESULTS AND DISCUSSIONS

A. Atomic structures and stability

Figures 1(a) and 1(b) shows the crystal structure of the SL CrXY ($X = S, Se, Te, Y = F, Cl, Br, I$). SL CrXY possess a hexagonal cell with space-group P3M1 (No.156) and its unit cell consists of three types of atoms, namely Cr, X, and Y, with the Cr atomic layer is sandwiched between the X and Y atomic layers. Each Cr atom pairs with three X atoms and three Y atoms, respectively, forming a trigonal prismatic geometry as shown in Fig. 1(a). The presence of two different types of nonmagnetic atoms breaks the spatial inversion symmetry of the system and lays the foundation for the generation of energy valley effect. The details about the lattice parameters of the SL CrXY are summarized in Table SI. In order to see the feature of charge transfer, the calculated differential charge densities and transferred charges by the Bader charge analysis are shown in Figs. 1(c) and S1 in the Supplemental Material [58]. As the electronegativity of Y atoms decreases, electrons will be more inclined to transfer to X atoms. It can be seen that as the electronegativity of Y (F, Cl, Br, I) atoms decreases, electrons will be more inclined to transfer to X (S, Se, Te) atoms. Due to unequal transfer of electrons near Cr towards X and Y atoms, a vertical polarization crucial for piezoelectric properties is generated.

We determine the magnetic ground state of CrXY by comparing the energies of its FM and antiferromagnetic (AFM) states with the supercell of $4 \times 4 \times 1$. Three magnetic configurations of AFM for SL CrXY are shown in Figs. 1(e)–1(g), respectively. The calculated energy differences ΔE can be defined as

$$\Delta E = E_{\text{AFM}} - E_{\text{FM}}, \quad (1)$$

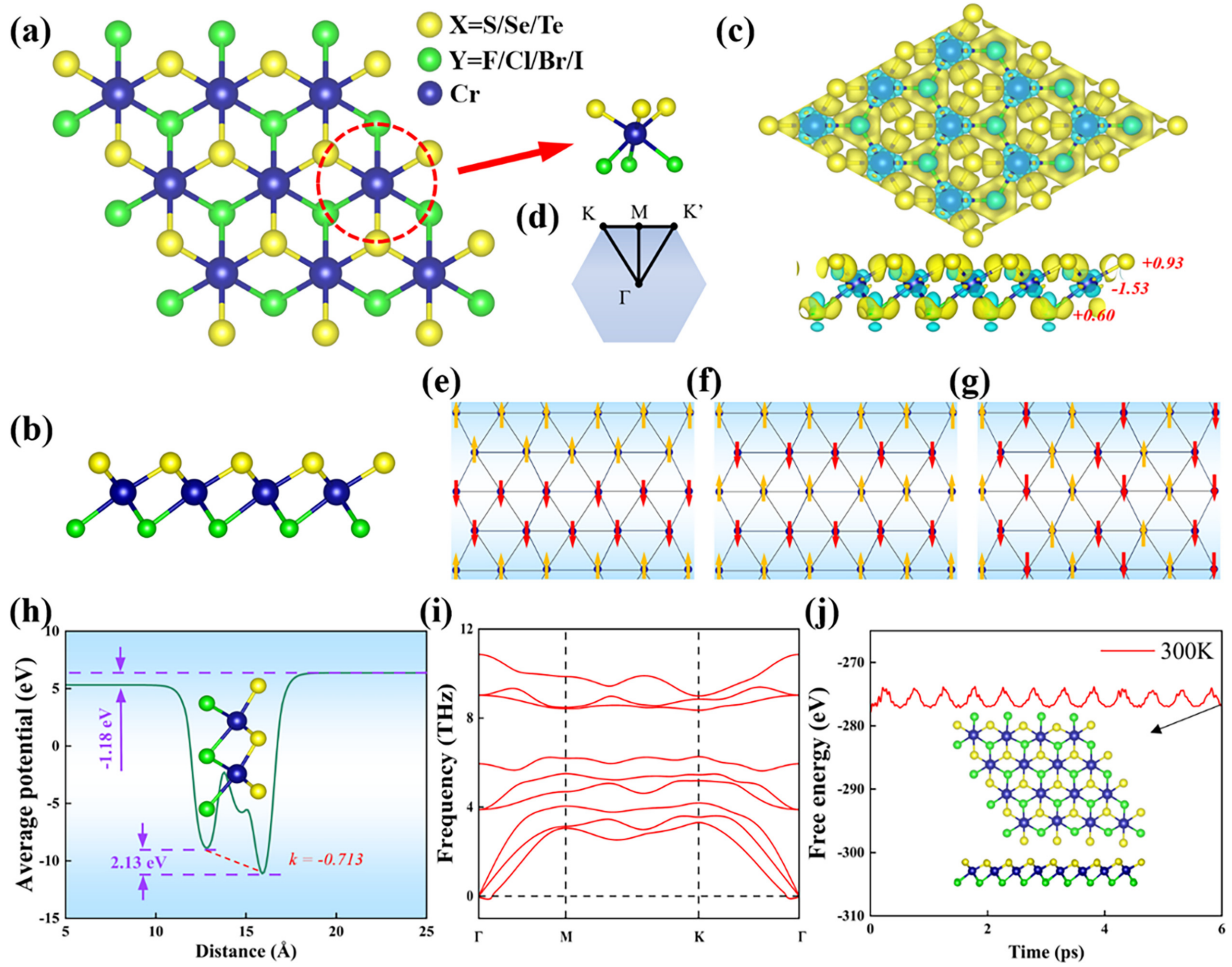


FIG. 1. (a) Top and (b) side views of the SL CrXY. The unit cell is marked by the red dashed lines. (c) The differential charge densities of SL CrSBr, and the red number represents the result of transferred charges. (d) The schematic diagram of the first Brillouin zone (BZ). (e) AFM1, (f) AFM2, and (g) AFM3 states of crystal structures, and the orange (red) arrow shows the direction of spin-up (spin-down). (h) Planar average electrostatic potential energy, and the slope of the red dashed line corresponds to the intrinsic electric field ($\text{eV}/\text{\AA}$) of SL CrSBr. (i) The phonon dispersion of SL CrSBr. (j) The fluctuation of total energy and snapshots of geometric structures for SL CrSBr at 300 K.

where E_{FM} and E_{AFM} represent the energies of SL CrXY unit cell on the FM and AFM states, respectively. Table SI shows the energy difference ΔE between FM and AFM of magnetic SL CrXY, indicating that the FM state is the ground state of SL CrXY because its lower energy than the AFM state. The ferromagnetic coupling in SL CrXY can be explained by the competition between the Cr-Cr direct-exchange and Cr-X(Y)-Cr superexchange interactions. Taking SL CrSBr as an example, the distance (d_1) between two neighboring Cr atoms is 3.52 \AA , while the distance ($d_2(d_3)$) between Cr and S(Br) atoms is $2.35(2.62) \text{ \AA}$. The distance of d_1 is larger than that of $d_2(d_3)$, indicating that the direct coupling among Cr atoms should be weak. However, the angle of Cr-S-Cr bond and Cr-Br-Cr bond are 97.07° and 84.16° , respectively, which is close to 90° . Based on Goodenough-Kanamori-Anderson rules [59–61], in SL CrSBr, the FM superexchange interaction is strong, which leads to FM coupling between Cr atoms. Then, take SL CrSBr as an example to discuss the average electrostatic potential in SL CrXY, the calculated result is shown in Figs. 1(h) and S2. The calculated average electrostatic potential along the z axis is asymmetric with a potential drop of 2.13 eV . In the sandwich structure, the potential

difference between the upper and lower atoms means the change of the work function. On the Br side, the potential energy is smaller and work function is smaller than those on the S side, which is related to the smaller electronegativity of S atom. In addition, the electrostatic potential difference of 1.18 eV indicates the charge redistribution in SL CrSBr and the existence of out-of-plane dipole moment. The inherent electric field k of SL CrSBr with a value of $-0.713 \text{ eV}/\text{\AA}$ can be obtained from the slope of the plane average electrostatic potential between the outermost atoms. Both the out-of-plane dipole moment and the inherent electric field indicate internal polarization of the material, suggesting the possible existence of good piezoelectric properties.

The molecular dynamic calculation and phonon spectrum under different biaxial strains of SL CrXY are shown in Figs. 1, S3, and S4. The small energy fluctuations and the preservation of structural integrity revealed by AIMD indicate good thermal stability. The calculated phonon dispersion contains a negligible virtual frequency, which could be caused by phonon-magnetic coupling or strong electron correlations, thus the structure should be dynamically stable. It is worth noting that for SL CrTeF, there is no virtual frequency in its

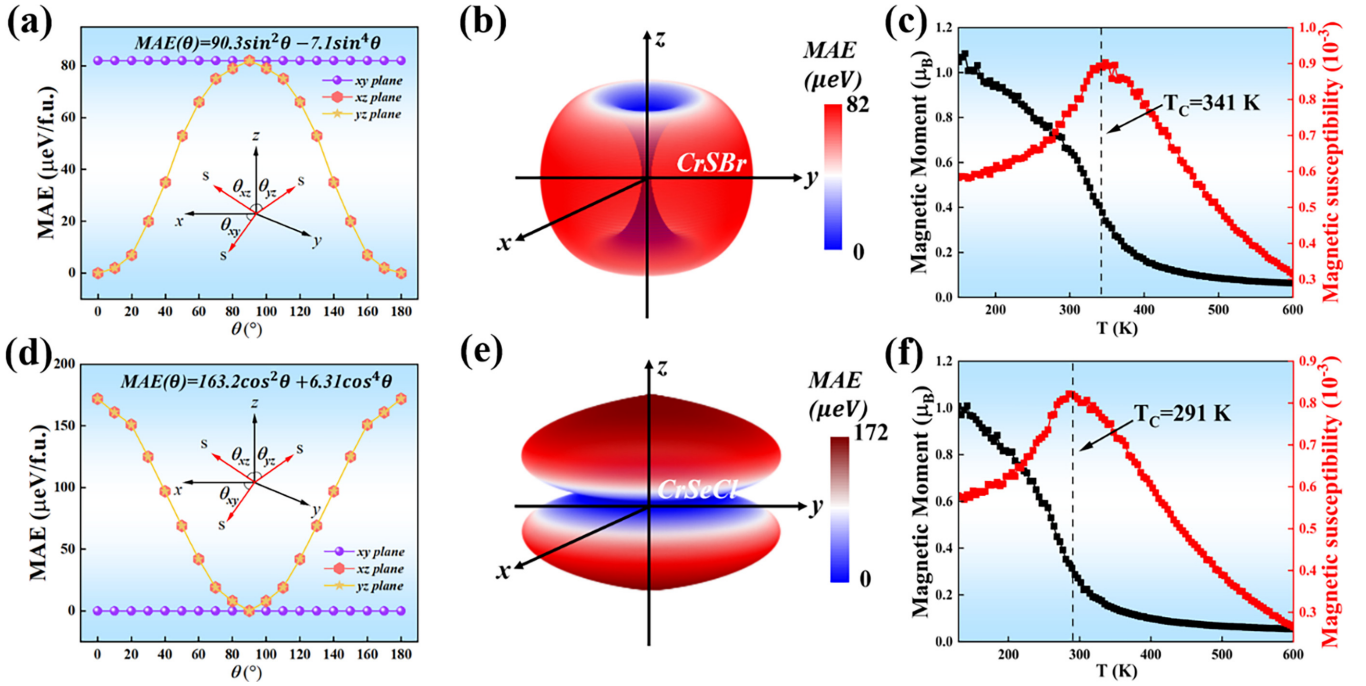


FIG. 2. (a) Dependence of MAE on the polar angle (θ) for the SL CrSBr with the direction of magnetization lying on xy , xz , and yz planes as well as (b) the whole space. (c) The temperature-dependent magnetic moments and magnetic susceptibility of SL CrSBr. (d) Dependence of MAE on the polar angle (θ) for the SL CrSeCl with the direction of magnetization lying on xy , xz , and yz planes as well as (e) the whole space. (f) The temperature-dependent magnetic moments and magnetic susceptibility of SL CrSeCl.

phonon spectrum and AIMD also shows small energy fluctuations. However, it can be seen from the illustration that its structural integrity is destroyed at 300 K, which restricts the application of SL CrTeF. Based on this, we will no longer discuss the properties of SL CrTeF.

B. Magnetic properties and T_c

MAE describing the magnetic anisotropy plays a crucial role in the long-range magnetic ordering of materials [62]. To determine MAE of SL CrXY, we calculate the energy in the magnetic moments of x axis and z axis of Cr atoms when the SOC effect is considered. The MAE is calculated by $\text{MAE} = E_{[001]} - E_{[100]}$ and the corresponding values are shown in Table SI, where $E_{[001]}$ and $E_{[100]}$ represent the outside plane and in-plane energy. Figures 2 and S5 shows the MAE of SL CrXY along xy , xz , and yz planes. Taking SL CrSBr and SL CrSeCl as examples, the MAE of SL CrSBr is $-82 \mu\text{eV}$, showing a perpendicular magnetic anisotropy (PMA) character, and the MAE of $172 \mu\text{eV}$ implies the in-plane magnetic anisotropy (IMA) character for the SL CrSeCl. Obviously, the MAE of SL CrXY exhibit strong dependence on the magnetization direction along the xz and yz planes, while it is not dependent on the xy plane. The MAE as a function of angle θ can be expressed as [63]

$$\text{MAE}(\theta) = K_1 \sin^2 \theta + K_2 \sin^4 \theta, \quad (2)$$

and

$$\text{MAE}(\theta) = K_3 \cos^2 \theta + K_4 \cos^4 \theta, \quad (3)$$

where $K_1(K_2)$ and $K_3(K_4)$ are the anisotropy constants and the angle θ takes the values of 0° to 180° . For the SL CrSBr, the

best fitting data ($K_1 > 0$ and $K_1 \gg K_2$) of MAE dependence on θ show a magnetization direction along out-of-plane axis. While, for SL CrSeCl, both K_3 and K_4 are positive, indicating that the MAE prefer a single easy axis. The above strong magnetic anisotropy is also proved by the distribution of MAE in the whole space as show in Figs. 2 and S6. The out-of-plane magnetization, which is great important for 2D ferrovalley materials, may be realized in the SL CrSeCl by artificially using an out-of-plane magnetic field to overcome the energy barrier of $172 \mu\text{eV}$ as shown in Fig. 2(d). We investigate the effect of biaxial strain on MAE, as shown in Fig. S7. It can be found that tensile strain can effectively enhance the ferromagnetism of SL CrXY. For example, the easily magnetized axis of SL CrSeBr can be transferred from in-plane to outside plane through strain adjustment, which is conducive to the generation of spontaneous valley polarization.

The T_c determines whether a ferromagnetic material has a practical application value. MC simulation based on the Heisenberg model is used to calculate and evaluate the T_c of ferromagnetic SL CrXY. When the mean magnetic moment of the system drops sharply to almost zero and the magnetic susceptibility increases to its maximum, the temperature at this time is confirmed to be the T_c . The spin Hamiltonian under the Heisenberg model can be expressed as [64]

$$H = -J \sum_{i,j} S_i \cdot S_j - A \sum_i (S_i^z)^2, \quad (4)$$

where J , S , and A are the Heisenberg exchange parameter, spin quantum number ($|S| = 1.5$), and MAE, respectively. The AFM configuration of the supercell for the calculation of the relevant T_c is shown in Figs. 1(e) and 1(f). By comparing

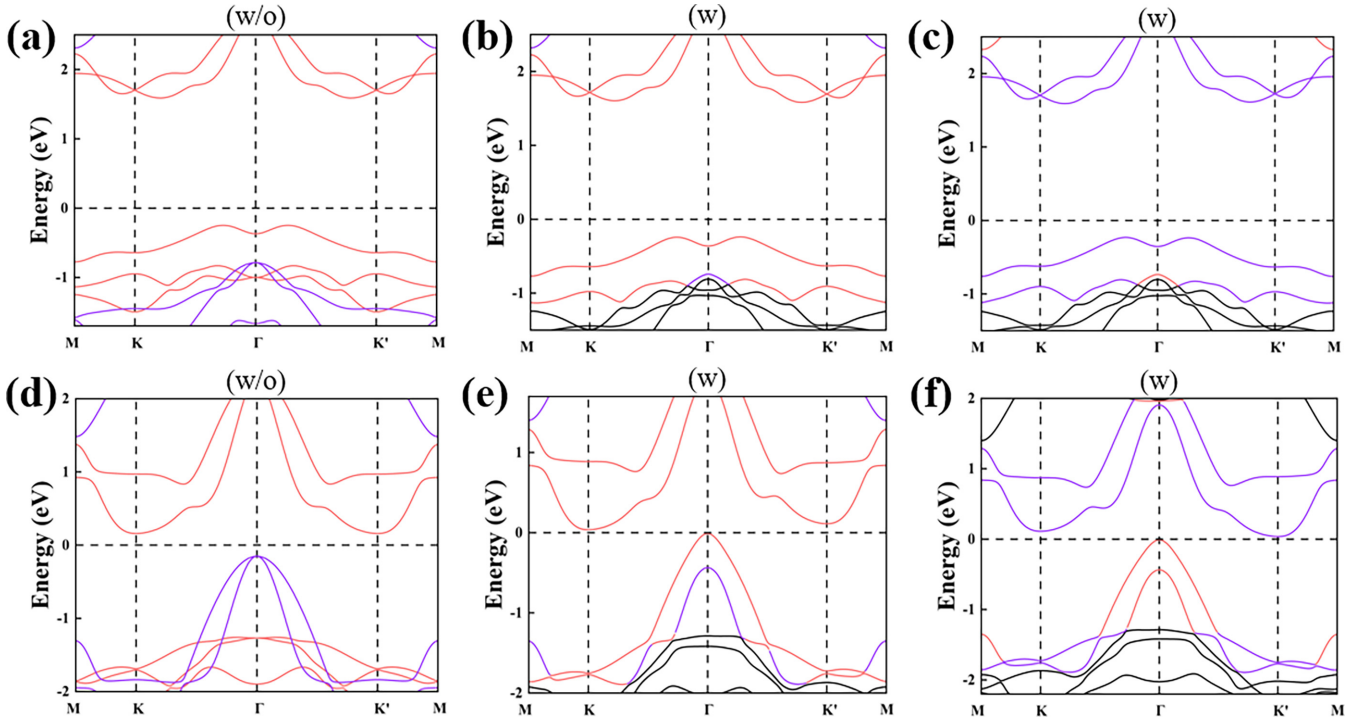


FIG. 3. The electronic band structures of SL CrSCl without SOC (a), (b) and (c) with SOC for the magnetic moment of Cr atom along $+z$ and $-z$. The electronic band structures of SL CrTeCl without SOC (d), (e), and (f) with SOC for the magnetic moment of Cr atom along $+z$ and $-z$. The red and purple lines represent the spin-up and spin-down states, respectively. The Fermi level is set to zero.

the energy of E_{FM} and E_{AFM} under different magnetic configurations of SL CrXY with the $4 \times 4 \times 1$ rectangle supercell, the J is determined from the following equations:

$$\begin{aligned} E(FM) &= E_0 - 3J_1S^2 - 3J_2S^2, \\ E(AF M1) &= E_0 - J_1S^2 + J_2S^2, \\ E(AF M2) &= E_0 + J_1S^2 + J_2S^2, \end{aligned} \quad (5)$$

where E_0 is the energy without magnetic coupling. Taking the Metropolis algorithm, we use the 44×44 supercells for MC simulation, and all relevant simulations are implemented in the code of MCSLOVER. The relevant J values of SL CrXY are shown in Table SI, and $J_1 > 0$ indicates that the magnetic interactions between the nearest neighbor Cr atoms are in FM state. Figs. 2(c), 2(f), and S8 shows the T_c is greater than 300 K for most SL CrXY. The large T_c of SL CrXY is far beyond those observed in the SL CrI₃ (45 K) [5] and VI₃ (49 K) [6] and strongly imply that they can be used as ideal ferromagnetic materials in valley electronic devices.

C. Electronic structures and valley polarization

The calculated electronic band structures of SL CrXY with (w) and without (w/o) SOC are shown in Figs. 3 and S9–S12. We can find that SL CrSCl, CrSeCl, CrSeBr and CrTeI have the characteristics of multiple energy valleys, where the un-equivalent energy valleys are located on high symmetric paths in momentum space [such as the electronic band structures of SL CrSCl shown in Figs. 3(a)–3(c)], while the energy valleys of other materials are located at high symmetric points [as shown in the electronic band structures of SL CrTeCl in Figs. 3(d)–3(f)]. So, we believe that SL CrXY belong to

valleytronic materials. One can find that SL CrSF, CrSCl, CrSBr, CrSI, and CrSeI are half-semiconductor (the bandgap values are displayed in Table SII) with valence band maximum (VBM) and conduction band minimum (CBM) possessing the same spin channel. Taking SL CrSCl in Figs. 3(b) and 3(c) as an example, on the basis of artificially controlling the magnetic moment direction of Cr atoms, 100% spin polarized charge carriers with different spin directions can be efficiently obtained through optical excitation. Meanwhile, the large bandgap of such materials is also beneficial to the development of related electronic spin devices.

In order to further investigate the valley related properties of SL CrXY, the projected band structures with (w) SOC are calculated with the magnetic moment of Cr atom along the $+z$ direction, and the results are shown in Figs. 4 and S13. The valley states at the K and K' points are mainly originated from the two degenerate d_{xz} and d_{yz} orbitals of Cr. The VBM or its nearby energy bands are mainly composed of the d_{z^2} orbitals of Cr. The valley polarization is defined as the energy difference ΔE_c and ΔE_v between K and K' valley at CBM and VBM, respectively, where $\Delta E_{c(v)} = E_{Kc(v)} - E_{K'c(v)}$. We can see a tiny valley polarization ΔE_v of almost zero at VBM in CrSZ ($Z = F, Cl, Br$) while a big valley polarization ΔE_c with application potential at CBM for the n -type carrier in CrXY. For example, the maximum of ΔE_v in CrSCl is only -4.7 meV, and the maximum of ΔE_c in CrTeCl is up to -76.1 meV. The valley-polarized state located at CBM of SL CrXY is ideal for practical applications. As shown in Figs. 3(b), 3(c), 3(e), and 3(f), the energy between the K and K' valleys will be exchanged with the reversal of the magnetic moment of the Cr atom, while the magnitude of the valley polarization remains unchanged.

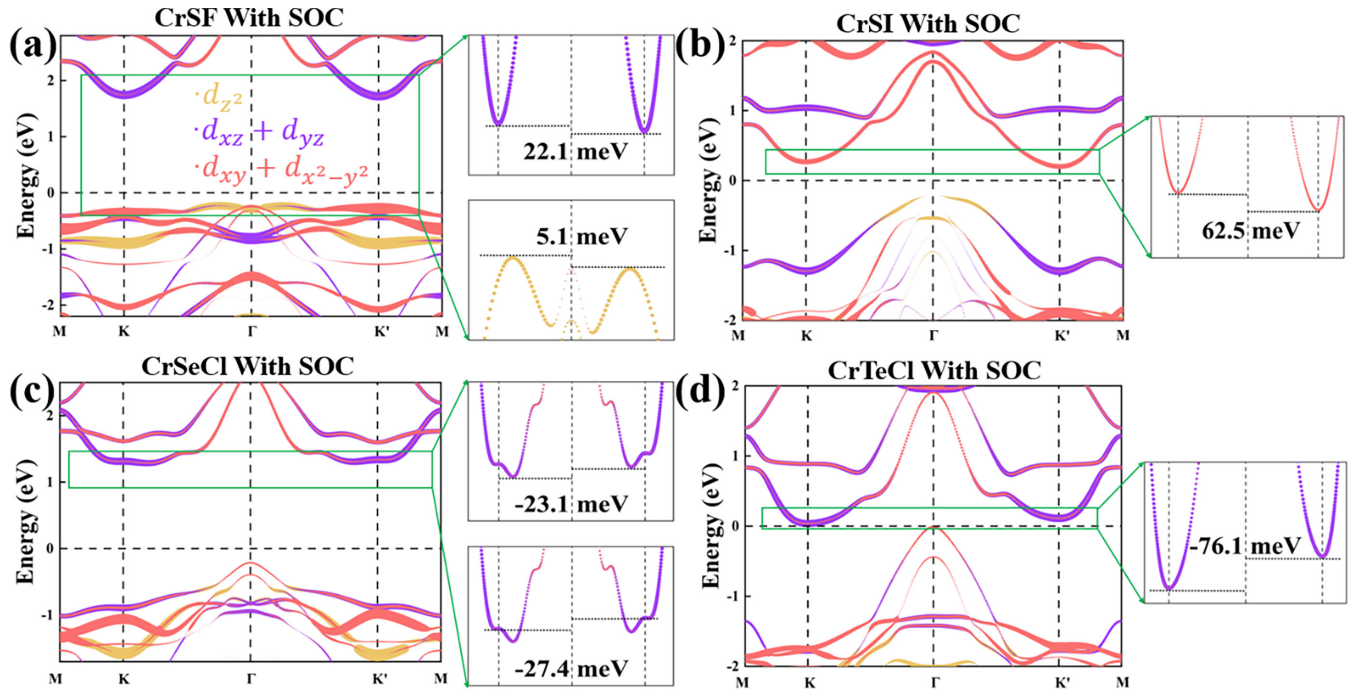


FIG. 4. The projected PBE electronic band structures for the (a) CrSF, (b) CrSI, (c) CrSeCl, and (d) CrTeF with considering SOC.

The valley polarization of CrXY is actually caused by the combined effects of intrinsic magnetic exchange field and SOC. When the SOC effect is not considered, it is found that under the influence of intrinsic magnetic exchange interaction, the spin up and spin down states are completely split, but the energy degeneracy between the K and K' valleys is not broken, i.e., $E_{\uparrow}(K) = E_{\uparrow}(K')$ and $E_{\downarrow}(K) = E_{\downarrow}(K')$. When including SOC effect but excluding intrinsic magnetic exchange field, the SOC effect will generate degenerate but not equivalent valleys at K and K', i.e., $E_{\uparrow}(K) = E_{\downarrow}(K')$ and $E_{\downarrow}(K) = E_{\uparrow}(K')$. Under both the intrinsic magnetic exchange field and SOC effect, the time inversion symmetry of SL CrXY is broken, and then the degeneracy between the energy valleys is broken. When we ignore the influence between spin up and spin down states, the Hamiltonian of SOC can be written as [65,66]:

$$H_{\text{SOC}} \approx H_{\text{SOC}}^0, \\ = \lambda S_z (L_z \cos \theta + \frac{1}{2} L_+ + e^{-i\phi} \sin \theta + \frac{1}{2} L_- e^{+i\phi} \sin \theta), \quad (6)$$

where L and S represent the orbital angular momentum and the spin angular momentum, respectively. θ is the magnetocrystalline angle:

$$L_+ = L_x + iL_y, \quad L_- = L_x - iL_y. \quad (7)$$

By orbital projection analysis, the basic functions can be chosen as: $|\psi_v\rangle = |d_{z^2}\rangle$, $|\psi_c^\tau\rangle = \frac{1}{\sqrt{2}}(|d_{xz}\rangle + i\tau|d_{yz}\rangle)$. Here, $\tau = \pm 1$ indicates the valley index at the K and K' valley. Therefore, the energy levels at VBM and CBM can be expressed as

$$E_v = \langle \psi_v | H_{\text{SOC}} | \psi_v \rangle, \quad E_c^\tau = \langle \psi_c^\tau | H_{\text{SOC}} | \psi_c^\tau \rangle \quad (8)$$

From the above, it can be concluded that the energy difference at VBM and CBM can be expressed as

$$\Delta E_v \approx 0, \\ \Delta E_c = i \langle d_{xz} | H_{\text{SOC}} | d_{yz} \rangle - i \langle d_{yz} | H_{\text{SOC}} | d_{xz} \rangle. \quad (9)$$

So, it is clear that introducing the SOC effect will break the energy degeneracy at CBM due to the nonzero value of ΔE_c , however, the energy degeneracy at VBM is almost not broken due to the almost zero valley of ΔE_v . The small valley polarization observed at the VBM of CrSF, CrSbI and CrSbBr is due to the fact that the energy band at the VBM is not solely composed of d_{z^2} orbitals. In short, intrinsic and spontaneous valley polarization in SL CrXY can overcome the drawbacks of methods such as magnetic doping and optical pumping that induce valley polarization.

D. Berry curvatures and AVHE

Under the Kubo formula [67], the Berry curvatures in the z direction can be derived as

$$\Omega_z(k) = \sum_n f_n \Omega_{n,z}(k), \quad (10)$$

in which f_n represents the Fermi-Dirac distribution, and $\Omega_{n,z}(k)$ can be obtained from

$$\Omega_{n,z}(k) = - \sum_{n \neq n'} \frac{2Im \langle \psi_{nk} | \hat{v}_x | \psi_{n'k} \rangle \langle \psi_{n'k} | \hat{v}_y | \psi_{nk} \rangle}{(E_n - E_{n'})^2}, \quad (11)$$

where $|\psi_{nk}\rangle$ is the Bloch wave function with eigenvalue E_n , and \hat{v}_x (\hat{v}_y) is the velocity operator along the x (y) direction.

Figures 5 and S14, shows the Berry curvatures of SL CrSI and CrXY along the high symmetry line and over the 2D

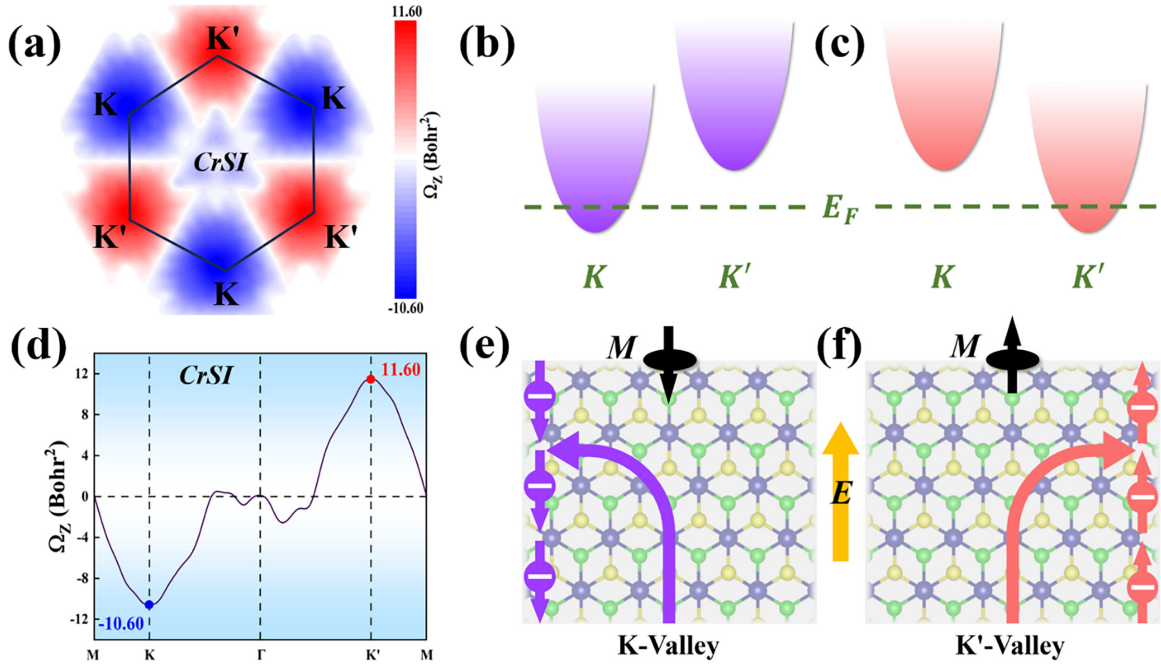


FIG. 5. (a) Contour map of Berry curvatures in the k space for SL CrSI. Diagrams of regulating Fermi energy levels in the $+z$ (b) and $-z$ (c) directions of magnetization under electron doping. (d) The Berry curvatures $\Omega(k)$ of SL CrSI as the curve along the high-symmetry path with the unit of Bohr². Diagram of the AVHE in SL CrSI when electrons are doped and in-plane electric field are applied in the $-z$ (e) and $+z$ (f) directions of magnetization. The purple and red balls with an arrow are spin-down and spin-up electrons, respectively.

Brillouin zone. Furthermore, based on the influence of different biaxial strains on the stability and band structures of the system, we calculated the Berry curvatures in k space under different strains (as shown in Figs. S15–S17). It can be seen that the Berry curvatures exhibits opposite signs and unequal absolute values, and its distribution exhibits a C_{3v} symmetry. Away from the K and K' valley, the Berry curvatures decays rapidly and disappears at the M points. Under a transverse electric field, the Bloch electrons will obtain an anomalous velocity [68]:

$$v_{\perp} = \frac{1}{\hbar} \frac{\partial E_n(k)}{\partial k} + \dot{k} \times \Omega_z(k). \quad (12)$$

Due to the large valley polarization, by doping electrons, we can move the Fermi level and adjust it to a certain valley at CBM without touching another valley, so as to selectively excite electrons in different valleys. At the same time, by adjusting the magnetization direction of Cr atoms to reverse valley polarization, the sign of Berry curvatures between energy valleys exchange while maintaining the same size. In this way, we can selectively detect the transverse voltage with opposite sign (negative voltage) on both sides of the sample. Take SL CrSI as an example, as plotted in Fig. 5(e), when the magnetization direction of Cr is the $-z$ axis, under the action of an in-plane electric field, the spin down carriers at the K valley will converge on the left side of the sample. If the magnetization direction is changed to $+z$ axis through external control, as plotted in Fig. 5(f), the spin up carriers will become the dominant carriers and converge on the right side of the sample, producing opposite Hall voltage.

E. Strain induced QAVHE

The development of hydrostatic pressure and nonconducting atomic force microscopy makes it possible to apply local stress to the sample. We investigate the ferromagnetism and electronic band structure of SL CrXY under biaxial strain within -6% – 6% . As shown in Fig. S18, valley splitting is significantly regulated by biaxial strain, especially for the valley splitting of SL CrSBr, CrSI, CrSeI, and CrTeX ($X = \text{Cl, Br, I}$) at CBM and the valley splitting of SL CrSX ($X = \text{F, Cl, Br, I}$) at the VBM. Taking SL CrSI as an example (as shown in Fig. S19), when the applied strain is less than 2% , there is no valley splitting at the VBM. When the strain is greater than 2% , there is about 35 meV valley splitting at the VBM. This result can be explained by the different superposition of atomic orbitals as a result of the changes in atomic bond length and bond angle by biaxial tensile strain [69]. Under the 6% tensile strain, almost -100 meV valley splitting can be observed in SL CrTeCl and CrTeBr, and 90 meV valley splitting can be observed in CrSeI.

Interestingly, when compressive strain is applied, the ferrovalley materials such as SL CrSI and CrTeX ($X = \text{Cl, Br, I}$) can be transformed into quasi-half-valley metals (quasi-HVM) (see Fig. 6). In quasi-HVM, the Fermi level slightly penetrates the VBM at Γ valley and the CBM at K or K' valley, and the Berry curvatures located in the BZ only occurs around K and K' valleys with opposite signs and unequal magnitudes. Under the combined action of the in-plane electric field and nonzero Berry curvatures, the carrier of K or K' valley can obtain the general group velocity v_{\parallel} and the anomalous transverse velocity v_{\perp} . However, the carrier of Γ valley can only obtain the general group velocity v_{\parallel} . As shown in Figs. 6(b) and 6(e), taking SL CrTeBr and SL CrSI as exam-

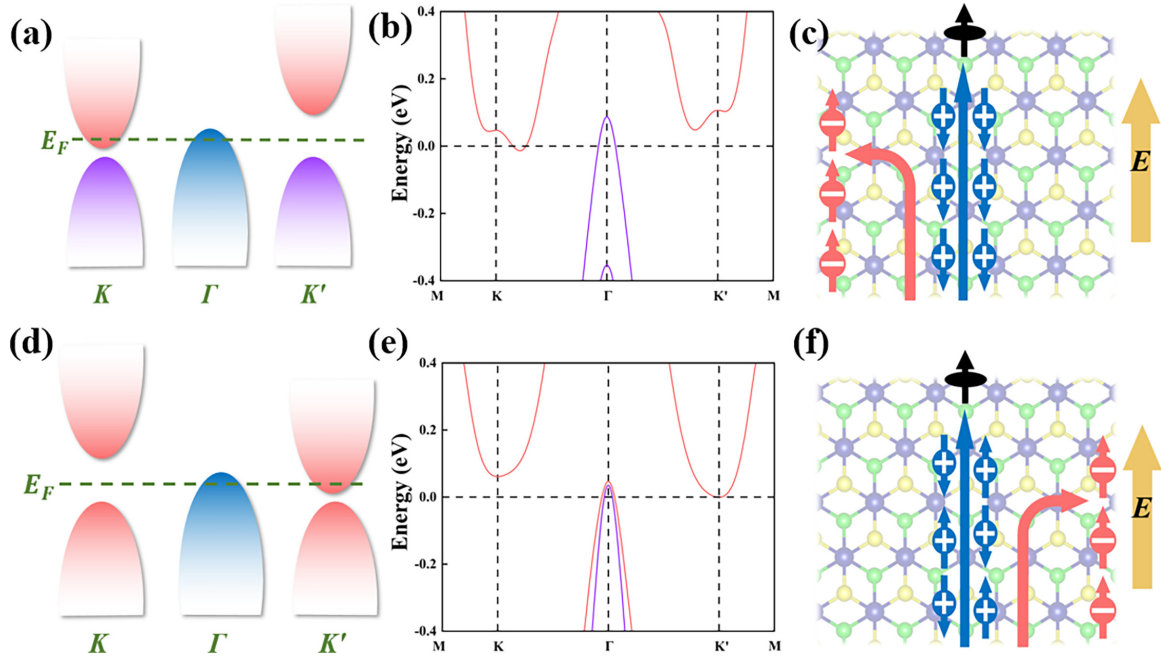


FIG. 6. (a) The illustration of band structure of quasiHVM with Fermi energy levels penetrating the K valley. (b) The band structure of SL CrTeBr under -5% strain. (c) Schematic illustration of quasiAVHE for SL CrTeBr. (d) The illustration of of band structure of quasiHVM with Fermi energy levels penetrating the K' Valley. (e) The band structure of SL CrSI under -6% strain. (f) Schematic illustration of quasiAVHE for SL CrSI.

ples, under the influence of stress, the Fermi level penetrates Γ valley, while it runs through the CBM of CrTeBr and CrSI located at K and K', respectively. In SL CrTeBr (CrSI), the spin up electron carriers contributed by the K (K') valley converge to the left(right) side of the sample, while hole carriers from Γ valley move in the direction of the electric field. Due to the fact that the Bloch electrons have transverse anomalous velocity similar to the AVHE while the hole carriers possess longitudinal velocity, this effect separating electron and hole carriers is called the quasi-AVHE. In addition to the applied strain, with the influence of the Hubbard correlation strength U , SL CrTeCl, and SL CrTeBr can be transformed into quasi-HVM. Figures S1—S12 shows the related band structure of SL CrXY when U value varies from 1.1 to 4.1 eV.

F. Piezoelectric properties

Owing to the semiconductor properties of the system and the breaking of spatial inversion symmetry, when a strain along the x axis is applied, the Janus SL CrXY can show both in-plane and out-of-plane piezoelectric properties ($e_{11}/d_{11} \neq 0$ and $e_{31}/d_{31} \neq 0$). Because the Janus SL CrXY belongs to P3M1 group symmetry, using the Voigt symbol, the piezoelectric tensor e_{ik} can be expressed as [42]

$$e = \begin{pmatrix} e_{11} & -e_{11} & 0 \\ 0 & 0 & -e_{11} \\ e_{31} & e_{31} & 0 \end{pmatrix}. \quad (13)$$

The elastic constant C_{ik} can be expressed as

$$d = \begin{pmatrix} d_{11} & -d_{11} & 0 \\ 0 & 0 & -2d_{11} \\ d_{31} & d_{31} & 0 \end{pmatrix}. \quad (14)$$

The piezoelectric coefficient d_{ik} has the following relationship with piezoelectric coefficient tensor e_{ik} and elastic coefficient C_{ik} :

$$e_{ik} = d_{ij}C_{jk}. \quad (15)$$

e_{ik} can be calculated by DFPT, and C_{ik} can be calculated based on the SSR, and the in-plane and out-of-plane piezoelectric coefficients can be expressed as

$$d_{11} = \frac{e_{11}}{C_{11} - C_{12}}, \quad d_{31} = \frac{e_{31}}{C_{11} + C_{12}}. \quad (16)$$

We use orthorhombic supercell (see Fig. S20) to calculate the e_{11} and e_{31} of SL CrXY. From the calculated elastic constants, we can conclude that they are mechanically stable because they satisfy the Born-Huang criteria [70], i.e., $C_{11} > 0$, $C_{11}C_{22} > C_{12}^2$ and $C_{33} > 0$. The piezoelectric stress coefficients (e_{11} and e_{31}) contributed by the ions and electrons, respectively, are plotted in Fig. S21. The piezoelectric stress coefficients e_{31} mainly come from the contribution of electrons and the signs for the contributions of electrons and ions in SL CrXY are generally opposite. Based on Eq. (16), the piezoelectric strain coefficients d_{11} and d_{31} are attained, and the relevant data are collected in Table I. The small e_{11} and d_{11} for SL CrXY are far less than those of the pristine and the Janus SL TMDs, indicating that SL CrXY exhibits smaller in-plane piezoelectricity. However, due to the significant charge transfer between X and Y atoms, the maximum e_{31} of SL CrXY can reach -2.76×10^{-10} C/m, which is much higher than the Janus MoSSe (0.02×10^{-10} C/m). Considering that $C_{11} - C_{12}$ and $C_{11} + C_{12}$ have smaller values, the maximum d_{31} in SL CrXY can reach -5.07 pV/m. Except for SL CrTeCl and CrTeBr, which can become metals with increasing U , all other materials are semiconductors within the

TABLE I. The elastic constants C_{ij} (Nm^{-1}), and the piezoelectric coefficients e_{ij} (10^{-10}C/m) and d_{ij} (pm/V) of SL CrXY.

Material	c_{11}	c_{12}	e_{11}	e_{31}	d_{11}	d_{31}
CrSF	71.89	17.74	1.92	-3.46	3.54	-3.86
CrSCL	63.72	14.12	0.61	1.97	1.23	2.53
CrSBr	61.83	13.62	-0.46	1.28	-0.96	1.69
CrSI	58.94	13.03	-0.21	0.28	-0.45	0.39
CrSeF	63.55	17.85	-2.64	-3.76	-5.78	-4.62
CrSeCl	54.81	12.91	-0.78	-2.40	-1.86	-3.55
CrSeBr	53.24	12.45	-0.63	-1.78	-1.55	-2.71
CrSeI	51.13	11.29	-0.45	-0.87	-1.14	1.39
CrTeCl	43.63	11.49	1.05	-2.77	3.27	-5.03
CrTeBr	42.75	10.81	0.76	-2.24	2.38	-4.19
CrTeI	41.90	9.79	0.58	-1.45	1.81	-2.81

considered U values. It is found that the piezoelectric coefficients (d_{11} and d_{31}) is robust against electronic correlation for SL CrXY (see Fig. S22). The d_{31} of SL CrSCL is the largest in SL CrSX ($X = \text{Cl, Br, I}$), and SL CrSeCl possesses the largest d_{31} among SL CrSeX ($X = \text{Cl, Br, I}$), and the d_{31} of SL CrTeCl is the largest among all materials we consider, which can be explained by considering the electronegativity difference (ED) between the upper and lower layers of atoms. As shown in Fig. 7, it can be observed that the ED between the X and Y atoms is positively correlated with the size of d_{31} . The above large out of plane piezoelectric coefficient (e_{31} and d_{31}) is crucial for the application of piezoelectric materials, indicating the excellent prospect of SL CrXY in piezoelectric applications.

IV. CONCLUSION

In summary, through first-principles calculations, we reveal that SL CrXY are 2D intrinsic FM materials with huge spin, valley and piezoelectric polarization. Ferrovalley SL CrXY has excellent dynamic/thermal stability and the estimated T_c of most of SL CrXY is greater than 300K. PMA and IMA can be found in SL CrXY, and for materials exhibiting IMA, the magnetization direction can be forced to change from in-plane to out-plane by artificially applying

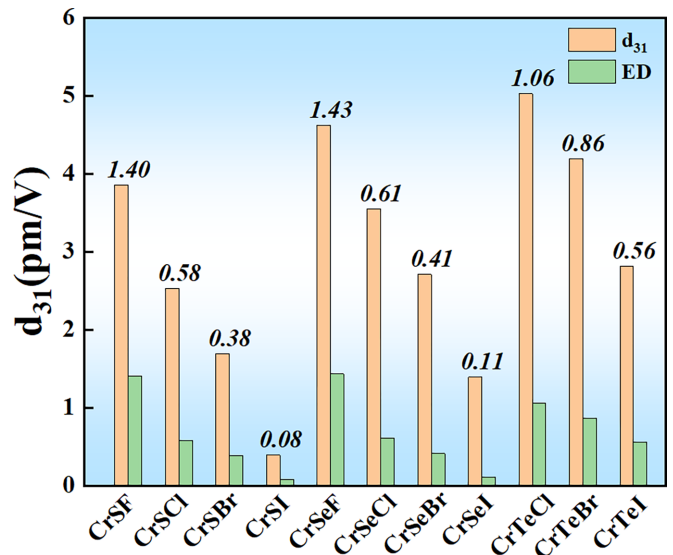


FIG. 7. The piezoelectric strain coefficients d_{31} of SL CrXY ($X = \text{S, Se, Te, and } Y = \text{Cl, Br, I}$) and the ED between the X and Y atoms. The value of ED is given in the chart, in the bar chart.

an external magnetic field. The maximum valley polarization of up to 76.1 meV can be found in CrTeCl, and valley polarization exceeding 90 meV can be found in CrSI, CrSeI, CrTeCl, and CrTeBr at 6% tensile strain. Due to the breaking of time-reversal and inversion symmetry, nonzero out-of-plane Berry curvatures can be observed. The AVHE that exhibit valley-contrasting feature and quasi-AVHE that can be used to separate electrons and holes can be detected with an in-plane longitudinal electronic field. In addition, the in-plane piezoelectric constants d_{11} is predicted to be $-5.78 - 3.54 \text{ pm/V}$. The piezoelectric constants d_{31} is predicted to be $-5.03 - 2.53 \text{ pm/V}$. The large valley polarization and piezoelectric coefficient make SL CrXY has potential multifunctional application in spin/valleytronic devices and piezoelectrics.

ACKNOWLEDGMENT

We would like to acknowledge the support from the Natural Science Foundation of Hebei Province (No. A2020202010).

- [1] X. Tang and L. Kou, *J. Phys. Chem. Lett.* **10**, 6634 (2019).
- [2] J. Chu, Y. Wang, X. Wang, K. Hu, G. Rao, C. Gong, C. Wu, H. Hong, X. Wang, K. Liu *et al.*, *Adv. Mater.* **33**, 2004469 (2021).
- [3] Z. Liu, L. Deng, and B. Peng, *Nano Res.* **14**, 1802 (2021).
- [4] N. D. Mermin and H. Wagner, *Phys. Rev. Lett.* **17**, 1133 (1966).
- [5] B. Huang, G. Clark, E. Navarro-Moratalla, D. R. Klein, R. Cheng, K. L. Seyler, D. Zhong, E. Schmidgall, M. A. McGuire, and D. H. Cobden, *Nature (London)*, **546**, 270 (2017).
- [6] T. Kong, K. Stolze, E. I. Timmons, J. Tao, D. Ni, S. Guo, Z. Yang, R. Prozorov, and R. J. Cava, *Adv. Mater.* **31**, 1808074 (2019).
- [7] L. Cai, V. Tung, and A. Wee, *J. Alloys Compd.* **913**, 165289 (2022).
- [8] A. Rycerz, J. Tworzydło, and C. W. J. Beenakker, *Nat. Phys.* **3**, 172 (2007).
- [9] O. Gunawan, Y. P. Shkolnikov, K. Vakili, Z. Gokmen, E. P. De Poortere, and M. Shayegan, *Phys. Rev. Lett.* **97**, 186404 (2006).
- [10] Y. P. Shkolnikov, E. P. De Poortere, E. Tutuc, and M. Shayegan, *Phys. Rev. Lett.* **89**, 226805 (2002).
- [11] T. Zhang, S. Zhao, A. Wang, Z. Xiong, Y. Liu, M. Xi, S. Li, H. Lei, Z. V. Han, and F. Wang, *Adv. Funct. Mater.* **32**, 2204779 (2022).

- [12] T. Zhang, X. Xu, B. Huang, Y. Dai, and Y. Ma, *Npj Comput. Mater.* **8**, 64 (2022).
- [13] J. R. Schaibley, H. Yu, G. Clark, P. Rivera, J. S. Ross, K. L. Seyler, W. Yao, and X. Xu, *Nat. Rev. Mater.* **1**, 16055 (2016).
- [14] X. Xu, W. Yao, D. Xiao, and T. F. Heinz, *Nat. Phys.* **10**, 343 (2014).
- [15] G.-B. Liu, D. Xiao, Y. Yao, X. Xu, and W. Yao, *Chem. Soc. Rev.* **44**, 2643 (2015).
- [16] H.-Z. Lu, W. Yao, D. Xiao, and S.-Q. Shen, *Phys. Rev. Lett.* **110**, 016806 (2013).
- [17] H. Zeng, J. Dai, W. Yao, D. Xiao, and X. Cui, *Nat. Nanotechnol.* **7**, 490 (2012).
- [18] T. Cao, G. Wang, W. Han, H. Ye, C. Zhu, J. Shi, Q. Niu, P. Tan, E. Wang, B. Liu, and J. Feng, *Nat. Commun.* **3**, 887 (2012).
- [19] Y. Li, J. Ludwig, T. Low, A. Chernikov, X. Cui, G. Arefe, Y. D. Kim, A. M. van der Zande, A. Rigosi, H. M. Hill, S. H. Kim, J. Hone, Z. Li, D. Smirnov, and T. F. Heinz, *Phys. Rev. Lett.* **113**, 266804 (2014).
- [20] D. MacNeill, C. Heikes, K. F. Mak, Z. Anderson, A. Kormányos, V. Zólyomi, J. Park, and D. C. Ralph, *Phys. Rev. Lett.* **114**, 037401 (2015).
- [21] G. Aivazian, Z. Gong, A. M. Jones, R.-L. Chu, J. Y. an, D. G. Mandrus, C. Zhang, D. Cobden, W. Yao, and X. Xu, *Nat. Phys.* **11**, 148 (2015).
- [22] Y. C. Cheng, Q. Y. Zhang, and U. Schwingenschlögl, *Phys. Rev. B.* **89**, 155429 (2014).
- [23] J. Qi, X. Li, Q. Niu, and J. Feng, *Phys. Rev. B.* **92**, 121403(R) (2015).
- [24] T. Norden, C. Zhao, P. Zhang, R. Sabirianov, A. Petrou, and H. Zeng, *Nat. Commun.* **10**, 4163 (2019).
- [25] W.-Y. Tong, S.-J. Gong, X. Wan, and C.-G. Duan, *Nat. Commun.* **7**, 13612 (2016).
- [26] J. Liu, W.-J. Hou, C. Cheng, H.-X. Fu, J.-T. Sun, and S. Meng, *J. Phys. Condens. Matter* **29**, 255501 (2017).
- [27] P. Zhao, Y. Ma, C. Lei, H. Wang, B. Huang, and Y. Dai, *Appl. Phys. Lett.* **115**, 261605 (2019).
- [28] K. Sheng, H. K. Yuan, and Z. Y. Wang, *Phys. Chem. Chem. Phys.* **24**, 3865 (2022).
- [29] H. Huan, Y. Xue, B. Zhao, G. Gao, H. Bao, and Z. Yang, *Phys. Rev. B.* **104**, 165427 (2021).
- [30] L. Liang, Y. Yang, X. Wang, and X. Li, *Nano Lett.* **23**, 858 (2023).
- [31] R. Li, J. Jiang, W. Mi, and H. Bai, *Nanoscale.* **13**, 14807 (2021).
- [32] Y. L. Hong, Z. Liu, L. Wang, T. Zhou, and W. Ren, *Science.* **369**, 670 (2020).
- [33] L. Wang, Y. Shi, M. Liu, A. Zhang, Y.-L. Hong, R. Li, Q. Gao, M. Chen, W. Ren, H.-M. Cheng *et al.*, *Nat. Commun.* **12**, 2361 (2021).
- [34] K.-A. N. Duerloo, M. T. Ong, and E. J. Reed, *J. Phys. Chem. Lett.* **3**, 2871 (2012).
- [35] M. N. Blonsky, H. L. Zhuang, A. K. Singh, and R. G. Hennig, *ACS Nano.* **9**, 9885 (2015).
- [36] W. Wu, L. Wang, Y. Li, F. Zhang, L. Lin, S. Niu, D. Chenet, X. Zhang, Y. Hao *et al.*, *Nature (London).* **514**, 470 (2014).
- [37] R. Fei, W. Li, J. Li, and L. Yang, *Appl. Phys. Lett.* **107**, 173104 (2015).
- [38] P. Li, Z. Zhang, W. Shen, C. Hu, W. Shen, and D. Zhang, *J. Mater. Chem. A.* **9**, 4716 (2021).
- [39] S. Chen, Z. Zeng, B. Lv, S. Guo, X. Chen, and H. Geng, *Phys. Rev. B.* **106**, 115307 (2022).
- [40] D. Xiao, G.-B. Liu, W. Feng, X. Xu, and W. Yao, *Phys. Rev. Lett.* **108**, 196802 (2012).
- [41] Q. Zhang, S. Zuo, P. Chen, and C. Pan, *InfoMat.* **3**, 987 (2021).
- [42] L. Dong, J. Lou, and V. B. Shenoy, *ACS Nano.* **11**, 8242 (2017).
- [43] A. Lu, H. Zhu, J. Xiao, C. Chuu, Y. Han, M. Chiu, C. Cheng, C. Yang, K. Wei, Y. Yang *et al.*, *Nat. Nanotechnol.* **12**, 744 (2017).
- [44] J. Zhang, S. Jia, I. Kholmanov, L. Dong, D. Er, W. Chen, H. Guo, Z. Jin, V. Shenoy, L. Shi *et al.*, *ACS Nano.* **11**, 8192 (2017).
- [45] P. E. Blöchl, *Phys. Rev. B.* **50**, 17953 (1994).
- [46] G. Kresse and D. Joubert, *Phys. Rev. B.* **59**, 1758 (1999).
- [47] G. Kresse and J. Furthmüller, *Phys. Rev. B.* **54**, 11169 (1996).
- [48] G. Kresse and J. Furthmüller, *Comput. Mater. Sci.* **6**, 15 (1996).
- [49] J. P. Perdew, K. Burke, and M. Ernzerhof, *Phys. Rev. Lett.* **77**, 3865 (1996).
- [50] A. I. Liechtenstein, V. I. Anisimov, and J. Zaanen, *Phys. Rev. B* **52**, R5467 (1995).
- [51] S. D. Guo, X. S. Guo, Y. T. Zhu, and Y. S. Ang, *Appl. Phys. Lett.* **121**, 062403 (2022).
- [52] S. Steiner, S. Khmelevskiy, M. Marsmann, and G. Kresse, *Phys. Rev. B* **93**, 224425 (2016).
- [53] V. Wang, N. Xu, J.-C. Liu, G. Tang, and W.-T. Geng, *Comput. Phys. Commun.* **267**, 108033 (2021).
- [54] A. Togo, F. Oba, and I. Tanaka, *Phys. Rev. B* **78**, 134106 (2008).
- [55] D. Bucher, L. C. T. Pierce, J. A. McCammon, and P. R. L. Markwick, *J. Chem. Theory Comput.* **7**, 890 (2011).
- [56] L. Liu, X. Ren, J. H. Xie, B. Cheng, W. K. Liu, T. Y. An, H. W. Qin, and J. F. Hu, *Appl. Surf. Sci.* **480**, 300 (2019).
- [57] A. A. Mostofi, J. R. Yates, Y.-S. Lee, I. Souza, D. Vanderbilt, and N. Marzari, *Comput. Phys. Commun.* **178**, 685 (2008).
- [58] See Supplemental Material at <http://link.aps.org/supplemental/10.1103/PhysRevB.109.125413> for more details on the mechanical, magnetic, electronic and piezoelectric properties of the systems.
- [59] J. B. Goodenough, *Phys. Rev.* **100**, 564 (1955).
- [60] P. W. Anderson, *Phys. Rev.* **115**, 2 (1959).
- [61] J. Kanamori, *J. Appl. Phys.* **31**, S14 (1960).
- [62] B. Shabbir, M. Nadeem, Z. G. Dai, M. Fuhrer, Q. K. Xue, X. L. Wang, and Q. L. Bao, *Appl. Phys. Rev.* **5**, 041105 (2018).
- [63] Y. Z. Abdullahi, Z. D. Vatansever, F. Ersan, U. Akinci, O. U. Akturk, and E. Akturk, *Phys Chem. Chem. Phys.* **23**, 6107 (2021).
- [64] K. Sheng, Z.-Y. Wang, H.-K. Yuan, and H. Chen, *New J. Phys.* **22**, 103049 (2020).
- [65] R. Peng, Y. Ma, X. Xu, Z. He, B. Huang, and Y. Dai, *Phys. Rev. B* **102**, 035412 (2020).
- [66] M.-H. Whangbo, E. E. Gordon, H. Xiang, H.-J. Koo, and C. Lee, *Acc. Chem. Res.* **48**, 3080 (2015).
- [67] D. J. Thouless, M. Kohmoto, M. P. Nightingale, and M. den Nijs, *Phys. Rev. Lett.* **49**, 405 (1982).
- [68] D. Xiao, M. C. Chang, and Q. Niu, *Rev. Mod. Phys.* **82**, 1959 (2010).
- [69] C.-H. Chang, X. Fan, S.-H. Lin, and J.-L. Kuo, *Phys. Rev. B* **88**, 195420 (2013).
- [70] R. C. Andrew, R. E. Mapasha, A. M. Ukpong, and N. Chetty, *Phys. Rev. B.* **85**, 125428 (2012).